UNIVERSITY OF HELSINKI REPORT SERIES IN PHYSICS

HU-P-D147

Studies of electronic structure by x-ray Raman and emission spectroscopy: applications to MgB$_2$ superconductors and high pressure physics

Aleksi Mattila

Division of X-Ray Physics
Department of Physical Sciences
Faculty of Science
University of Helsinki
Helsinki, Finland

ACADEMIC DISSERTATION

To be presented, with the permission of
the Faculty of Science of the University of Helsinki,
for public criticism in Auditorium E204
of the Department of Physical Sciences (Physicum),
Gustaf Hällströmin katu 2a, on October 27th 2007 at 12 o'clock.

Helsinki 2007

Supervisor:

Prof. Keijo Hämäläinen
Department of Physical Sciences
University of Helsinki
Helsinki, Finland

Pre-examiners:

Prof. Claudia Dallera
Dipartimento di Fisica
Politecnico di Milano
Milano, Italy

Prof. Risto Nieminen
Laboratory of Physics
Helsinki University of Technology
Espoo, Finland

Opponent:

Dr. Michael Krisch
European Synchrotron
Radiation Facility
Grenoble, France

Custos:

Prof. Keijo Hämäläinen
Department of Physical Sciences
University of Helsinki
Helsinki, Finland

Report Series in Physics HU-P-D147
ISSN 0356-0961
ISBN 978-952-10-3259-2 (printed version)
ISBN 978-952-10-3260-8 (pdf version)
http://ethesis.helsinki.fi
Helsinki University Printing House
Helsinki 2007

Preface

This thesis is based on research carried out at the Division of X-ray Physics of the Department of Physical Sciences at the University of Helsinki. The x-ray scattering experiments were performed at the beamline ID16 of the European Synchrotron Radiation Facility (ESRF) in Grenoble, France.

I would like to thank Prof. Juhani Keinonen for the opportunity to work at the Department of Physical Sciences. I thank Prof. Keijo Hämäläinen and Prof. Seppo Manninen for introducing me to the field of x-ray and synchrotron radiation science. I am especially grateful to my supervisor Prof. Keijo Hämäläinen for tutoring me from the very beginning of my university studies. His inspiration, support and excellent international contacts have been invaluable throughout this work. I would like to express my gratitude to Dr. Aleksi Soininen for many valuable discussions and for his contributions to the theoretical and computational aspects of this work. Special thanks go to Dr. Szabolcs Galambosi for the very pleasurable co-work especially during the visits to ESRF. I would also like to thank Dr. Kim Nygård and Dr. Mikko Hakala for stimulating discussions and the rest of the personnel of the Division of X-ray Physics for creating a nice working environment.

I would like to thank the personnel of the ESRF for help and support. In particular, I would like to thank Dr. Simo Huotari, Dr. György Vankó and Mr. Tuomas Pylkkänen for their hospitality and collaboration during the many synchrotron experiments in Grenoble. I would also especially like to acknowledge the many enlightening discussions and insight of Dr. Vankó on x-ray emission spectroscopy and thank him for the very enjoyable cooperation over the years on various experiments at beamline ID16.

I am greatly indebted to Prof. Abhay Shukla and Dr. Jean-Pascal Rueff for introducing me to the field of high pressure physics and for the long lasting collaboration. I am especially grateful to Prof. Shukla for providing me with the possibility to work at the Université Pierre et Marie Curie and I would very much like to thank him and Dr. Rueff for their kind hospitality during the time I spent in Paris.

I thank Prof. Frank de Groot for the help with the cluster multiplet program and Dr. Nikolai Zhigadlo and Dr. Janusz Karpinski for their fruitful collaboration on MgB_2 studies. I would also like to thank Dr. Christian Sternemann for discussions. I also wish to express my gratitude to all the co-authors contributing to the publications of this thesis.

But most of all, I would like to thank Kira for her support and patience over the past years and our children Aava and Oosa for providing me with plenty of other content in life besides work.

This research was funded by the Academy of Finland and the National Graduate School in Materials Physics. Additional financial support was obtained from the ESRF, the European Union through the Marie Curie mobility funds, the Finnish Academy of Science and Letters (through the Vilho, Yrjö, and Kalle Väisälä Foundation), L'Association Franco-Finlandaise pour la Recherche Scientifique et Technique, the University of Helsinki Funds and the Emil Aaltonen Foundation.

A. Mattila: Studies of electronic structure by x-ray Raman and emission spectroscopy: applications to MgB_2 superconductors and high pressure physics, 2007, 35 pages and appendices. University of Helsinki, Report Series in Physics, HU-P-D147.

Classification (INSPEC): A7870C, A7870E, A3470
Keywords: inelastic x-ray scattering, synchrotron radiation, x-ray emission, density of states, diamond anvil cell

Abstract

X-ray Raman scattering and x-ray emission spectroscopies were used to study the electronic properties and phase transitions in several condensed matter systems. The experimental work, carried out at the European Synchrotron Radiation Facility, was complemented by theoretical calculations of the x-ray spectra and of the electronic structure.

The electronic structure of MgB_2 at the Fermi level is dominated by the boron σ and π bands. The high density of states provided by these bands is the key feature of the electronic structure contributing to the high critical temperature of superconductivity in MgB_2. The electronic structure of MgB_2 can be modified by atomic substitutions, which introduce extra electrons or holes into the bands. X-ray Raman scattering was used to probe the interesting σ and π band hole states in pure and aluminum substituted MgB_2. A method for determining the final state density of electron states from experimental x-ray Raman scattering spectra was examined and applied to the experimental data on both pure MgB_2 and on $Mg_{0.83}Al_{0.17}B_2$. The extracted final state density of electron states for the pure and aluminum substituted samples revealed clear substitution induced changes in the σ and π bands. The experimental work was supported by theoretical calculations of the electronic structure and x-ray Raman spectra.

X-ray emission at the metal $K\beta$ line was applied to the studies of pressure and temperature induced spin state transitions in transition metal oxides. The experimental studies were complemented by cluster multiplet calculations of the electronic structure and emission spectra. In $LaCoO_3$ evidence for the appearance of an intermediate spin state was found and the presence of a pressure induced spin transition was confirmed. Pressure induced changes in the electronic structure of transition metal monoxides were studied experimentally and were analyzed using the cluster multiplet approach. The effects of hybridization, bandwidth and crystal field splitting in stabilizing the high pressure spin state were discussed. Emission spectroscopy at the $K\beta$ line was also applied to $FeCO_3$ and a pressure induced iron spin state transition was discovered.

List of publications

This thesis consists of an introductory part followed by six research papers, which are referred to by the roman numerals **I - VI** throughout the text.

I **A. Mattila**, J. A. Soininen, S. Galambosi, S. Huotari, G. Vankó, N. D. Zhigadlo, J. Karpinski, and K. Hämäläinen, *Local Electronic Structure of* MgB_2 *by X-ray Raman Scattering at the Boron K edge*, Physical Review Letters **94**, 247003 (2005)

II J. A. Soininen, **A. Mattila**, J. J. Rehr, S. Galambosi, and K. Hämäläinen, *Experimental determination of the core-excited electron density of states*, Journal of Physics: Condensed Matter **18**, 7327 (2006)

III **A. Mattila**, J. A. Soininen, S. Galambosi, T. Pylkkänen, S. Huotari, N. D. Zhigadlo, J. Karpinski, and K. Hämäläinen, *Electron hole counts in Al substituted* MgB_2 *from x-ray Raman scattering*, submitted to Physical Review B

IV G. Vankó, J.-P. Rueff, **A. Mattila**, Z. Németh, and A. Shukla, *Temperature- and pressure-induced spin-state transitions in* $LaCoO_3$, Physical Review B **73**, 024424 (2006)

V **A. Mattila**, J.-P. Rueff, J. Badro, G. Vankó, and A. Shukla, *Metal-ligand interplay in strongly correlated oxides: a parametrized phase diagram for pressure induced spin transitions*, Physical Review Letters **98**, 196404 (2007)

VI **A. Mattila**, T. Pylkkänen, J.-P. Rueff, S. Huotari, G. Vankó, M. Hanfland, M. Lehtinen, and K. Hämäläinen, *Magnetic transition of iron in siderite* $FeCO_3$ *mineral at high pressure*, Journal of Physics: Condensed Matter **19**, 386206 (2007)

The author of this thesis is the principal author of papers **I**, **III**, **V** and **VI** and a contributing author of papers **II** and **IV**. He is responsible for planning and conducting the experimental work and performing the data analysis in papers **I**, **III** and **VI**, and has participated actively to the experimental work and analysis of the results in paper **IV**. In paper **II** he has contributed significantly to the development of the methodology and performed the data analysis. He has performed the cluster multiplet calculations for papers **IV-VI** and participated in carrying out the multiple scattering calculations shown in papers **I-IV**.

Contents

1 Introduction

The study of x-ray scattering and absorption phenomena started with the discovery of x-rays by W. Röntgen in 1895 [1]. It was soon realized that two types of inelastic scattering phenomena were involved. The other scattering process produced radiation with a continuous spectrum, while the other one was characteristic radiation with the intensity and the discrete energy spectrum dependent on the elemental composition of the scatterer. This characteristic radiation is today commonly referred to as fluorescence radiation. The energies of the discrete fluorescence radiation were identified with the atomic energy levels of the Bohr model by Moseley 1913 [2] and the discovery was further systemized by Barkla, who noticed two separate sets of radiation, which he named K and L [3]. The relation between the energies of the fluorescence radiation and Bohr's atomic orbitals provided experimental support for the Bohr's atomic model and helped to pave way for the novel theory of quantum mechanics. Fluorescence radiation is also utilized in this thesis, where information about the electronic structure of the scattering system is obtained by high energy resolution measurements of the lineshape of this radiation.

The nature of the scattered radiation with the continuous spectrum was explained by the experiments of Compton [4] and Debye [5] by using the newly coined concept of light quantum to explain their results. Soon after, the novel Compton scattering was used to show that the valence electrons in beryllium metal followed the Fermi-Dirac distribution [6], with the experiment demonstrating the potential of inelastic x-ray scattering experiments in probing the electronic structure of matter. A few years before Compton's observations the existence of a fine structure in x-ray absorption spectrum and the relation of these intensity modulations to the chemical environment of the absorbing atom was discovered in the works of W. Stenström [7] and later especially by Fricke [8] and W. Kossel [9]. A notable development after the early days was the realization by Mizuno and Ohmura that inelastic scattering could be used to obtain the same information as x-ray absorption [10]. This so-called x-ray Raman scattering (XRS) regime is also used in this thesis.

With the later developments of quantum mechanics, the different x-ray scattering phenomena have been extensively used to probe various physical properties of matter. The early experiments were done using x-ray tubes and radioactive sources. Starting from the 1950's experimental work began to utilize synchrotron radiation that was at that time an unwanted byproduct of storage rings built for high energy particle physics. With the advent of second generation storage rings built specifically for synchrotron radiation production, the whole x-ray science was revolutionarized. This development work is culminating, from the x-ray scattering spectroscopy point of view, in the high resolution multi-element crystal spectrometers currently installed on the beamlines of third generation synchrotron radiation sources. The future advancements in the experimental field will involve x-ray free-electron laser sources currently under construction [11].

Alongside with the experimental developments driven by synchrotron radiation, the theoretical understanding of the properties of condensed matter and the scattering phenomena of x-rays has advanced considerably. Theoretical methods employing the increasing power of modern day computers have enabled us to understand from the first principles the ground state properties of a wide variety of condensed matter systems. Notable challenges still exist, including strongly correlated electronic systems or systems with crystal defects or substitutional compositions, which so far lack a complete theoretical understanding. Computational and theoretical modelling of the scattering phenomena of x-rays is, in many cases, also a demanding task due to the need to include the excited states of the electronic system into the description of the scattering process.

This thesis combines experiments utilizing synchrotron radiation based inelastic x-ray scattering spectroscopies together with advanced computational methods to study the electronic structure in condensed matter systems. These methods are applied to MgB_2 superconductors and studies of pressure and temperature induced phase transitions in $3d$ transition metal oxides.

This introductory part will be followed, in Section 2, by a short review of the theory of inelastic x-ray scattering. Section 3 will discuss the main computational methods employed in this work. Section 4 will describe experimental details and finally, in Sections 5 and 6, the main results of this thesis are summarized.

The unit system used in this thesis is the atomic unit (a.u.) system, where $\hbar = c = m_e = e = c\alpha = 1$ and α is the fine structure constant. The photon energies and energy transfers are, however, reported in electron volts (eV).

2 Inelastic X-ray Scattering

In inelastic x-ray scattering experiments incident x-ray photons with energy ω_1, momentum $\mathbf{k}_1$ and polarization state $\boldsymbol{\varepsilon}_1$ interact with the electron system, which is initially in state $|I\rangle$ with an energy E_I. The scattered photons have energy ω_2, momentum $\mathbf{k_2}$ and polarization state $\boldsymbol{\varepsilon}_2$. Energy $\omega = \omega_1 - \omega_2$ and momentum $\mathbf{q} = \mathbf{k}_1 - \mathbf{k}_2$ are transferred to the electron system in the scattering process. After the scattering process, the electron system is left in a state $|F\rangle$ with an energy E_F.

The measured quantity in inelastic x-ray scattering experiments is the double-differential scattering cross section given in the non-relativistic form by the Kramers-Heisenberg formula [12, 13]

$$
\begin{aligned}
\frac{d^2\sigma}{d\Omega d\omega_2} &= r_0^2\,\frac{\omega_2}{\omega_1}\sum_F |\langle F|\sum_i e^{i\mathbf{q}\cdot\mathbf{r}_i}|I\rangle(\boldsymbol{\varepsilon}_1\cdot\boldsymbol{\varepsilon}_2) \\
&- \sum_M [\frac{\langle F|\sum_i(\boldsymbol{\varepsilon}_1\cdot\mathbf{p}_i)e^{i\mathbf{k}_1\cdot\mathbf{r}_i}|M\rangle\langle M|\sum_i(\boldsymbol{\varepsilon}_2\cdot\mathbf{p}_i)e^{-i\mathbf{k}_2\cdot\mathbf{r}_i}|I\rangle}{E_M+\omega_2-E_I} \\
&+ \frac{\langle F|\sum_i(\boldsymbol{\varepsilon}_2\cdot\mathbf{p}_i)e^{-i\mathbf{k}_2\cdot\mathbf{r}_i}|M\rangle\langle M|\sum_i(\boldsymbol{\varepsilon}_1\cdot\mathbf{p}_i)e^{i\mathbf{k}_1\cdot\mathbf{r}_i}|I\rangle}{E_M-\omega_1-E_I-i\Gamma_M}]|^2 \\
&\times\delta(\omega+E_I-E_F),
\end{aligned}
\tag{1}
$$

where r_0 is the classical electron radius. The first term on the right hand side in the cross-section describes elastic and inelastic scattering, including XRS, while the third term with the resonant denominator represents the fluorescence (characteristic) radiation and other resonant inelastic scattering phenomena. The contributions from the resonant process are enhanced when ω_1 is close to E_I. The second term describes a scattering process, which would become resonant when the energy of the intermediate state is less than in the initial state. The summation for the last two terms is taken over all the possible intermediate states $|M\rangle$ of the scattering process, with energies E_M and lifetimes Γ_M. The summations inside the matrix elements are taken over all the electrons of the system, with positions $\mathbf{r}_i$.

Different scattering regimes, classified according to the energy and momentum transfers, can be identified [13]. The most interesting ones from the point of view of this thesis are the (i) *(non-resonant) scattering by inner shell excitations* (the XRS regime) and (ii) *resonant inner shell excitation regime.* In the x-ray Raman regime, the energy transfer ω is tuned over the binding energy of a core electron, whereas in the resonant inner shell excitation regime the incident photon energy ω_1 is close to a binding energy of a core electron. The main interest in the resonant inner shell excitations in this thesis is limited to the cases where the incident photon energies are sufficiently high to excite the inner shell electron to continuum like states and the core hole decay to a higher orbital is followed by an emission of a fluorescence photon. In the following, these two scattering regimes are discussed in more detail.

2.1 X-ray Raman Scattering

In XRS experiment the energy transfer ω is tuned over the binding energy of a core state and the core electron is excited to an empty electron state. This excited electron probes the environment of the absorbing atom and the scattering probability is sensitive to the density of the empty electron states in the final state of the scattering process *i.e.* in the presence of a core hole. In the x-ray Raman energy regime, the scattering cross section is given by the first term of the Kramers-Heisenberg formula, given by Eq. (1). The cross section can be written as

$$\frac{d^2\sigma}{d\Omega d\omega_2} = \left(\frac{d\sigma}{d\Omega}\right)_{Th} \sum_F |\langle F| \sum_i e^{i\mathbf{q}\cdot\mathbf{r}_i} |I\rangle|^2 \, \delta(\omega + E_I - E_F), \tag{2}$$

where $(d\sigma/d\Omega)_{Th} = r_0^2 \, (\omega_2/\omega_1) \, (\boldsymbol{\varepsilon}_1 \cdot \boldsymbol{\varepsilon}_2)$ is the Thomson scattering cross section and the second term is the dynamic structure factor

$$S(\mathbf{q}, \omega) = \sum_F |\langle F| \sum_i e^{i\mathbf{q}\cdot\mathbf{r}_i} |I\rangle|^2 \, \delta(\omega + E_I - E_F). \tag{3}$$

The partitioning of the XRS cross section in Eq. (2) into these two terms separates the electron-photon coupling strength, given by the Thomson scattering cross section, from the electron system related effects described by the dynamic structure factor.

The dynamic structure factor is connected to the dynamics and spatial distributions of density fluctuations of the electron system through a Fourier transformation of the electron density-density correlation function [14]. This connection is especially useful when the scattering is not limited to the core excitations and, for example, collective and single particle like valence excitations of the system are studied. Possibly more practical relation for XRS experiments, discovered by Mizuno and Ohmura [10], is the connection of the XRS cross section to the x-ray absorption cross section. If the energy transfer ω in Eq. (3) is replaced with the energy ω_1 of the incident photons and the momentum transfer vector $\mathbf{q}$ with the polarization vector ϵ_1, the dynamic structure factor would become proportional to the x-ray absorption cross section; the matrix elements for the two cross sections are actually the same in the small $\mathbf{q}$ limit (when $qr_0 \ll 1$) i.e. when dipole transitions are dominant. This relation has been demonstrated by experimental studies, for example, for the K absorption edges of boron [15] and lithium [16].

With single crystal samples, the *direction* of the momentum transfer vector $\mathbf{q}$ relative to the crystal orientation can be used to discriminate between contributions from final states with different spatial orientations, as in x-ray absorption through the direction of the polarization vector [17]. An interesting aspect of XRS experiments is that the *magnitude* of the momentum transfer vector $\mathbf{q}$ can be tuned. This offers the possibility to change the weight of the non-dipole transitions and eventually separate the contributions from final states with different symmetries, as discussed in more detail in the next section. One of the main experimental advantage of XRS over x-ray absorption is that the absorption edges of light elements can be accessed using hard x-rays. XRS a bulk sensitive technique and the hard x-rays also provide an access to various restrictive sample environments including diamond anvil cells [18, 19]. Soft x-ray edges of vacuum sensitive samples like liquids are also accessible using XRS [20].

Electron energy loss spectroscopy (EELS) [21,22] can be used to study same excitations which are accessible using x-ray Raman scattering. EELS technique offers some advantages over XRS. Generally, the energy resolution obtained in EELS experiments is somewhat better compared to XRS. Electron beams focused down to nm scale are also available. This allows one, for example, to focus the beam to a single crystal domain inside a polycrystalline sample to obtain directional information on the final state density of electron states [23]. EELS experiments can be performed using small laboratory scale instruments, compared to the synchrotron radiation sources needed for XRS measurements. A drawback is that measurements with high momentum transfer become difficult due the rapidly decreasing scattering cross section with increasing q. The strong interaction of the electrons in solids can also lead to multiple scattering, which complicates the analysis of the experimental results, besides rendering EELS technique surface sensitive. Nevertheless, the momentum transfer dependence of the EELS cross section has been successfully employed to obtain information beyond the dipole limit [24] similarly as in XRS.

2.2 Determining the Final State Electron Density of States

By considering the full operator $e^{i\mathbf{q}\cdot\mathbf{r}}$ in the XRS cross section given by Eq. (2), information beyond the dipole limit can be obtained in x-ray Raman experiments [25]. This is easily seen by expanding the exponential term as $e^{i\mathbf{q}\cdot\mathbf{r}} = 1+i\mathbf{q}\cdot\mathbf{r}+(i\mathbf{q}\cdot\mathbf{r})^2/2\ldots$. With increasing momentum transfer, the higher order terms in the expansion gain more weight and may start to contribute considerably to the cross section. [26–29]. This momentum transfer dependence can be exploited to separate the contributions from final states with different angular momenta to the XRS spectra, as shown in **papers I-III**.

A method to quantitatively separate the different final state components from the experimental XRS spectra has been recently proposed [30]. This method relies on a real space multiple scattering formulation of the XRS cross section. The dynamic structure factor can be approximated as a linear equation relating the final state empty partial local densities of states $\rho_L(E)$, where L is the angular momentum of the state, to the $S(\mathbf{q},\omega)$ through

$$S(\mathbf{q},\omega) = \sum_L |M_L(\mathbf{q},E)|^2 \rho_L(E). \tag{4}$$

The matrix elements $M_L(q,E)$ are essentially atomic quantities describing the transition from an initial core state to the final state with energy $E = \omega + E_I$. These matrix elements have smooth energy dependence and as atomic quantities can be calculated to a very good degree of accuracy. The essence of the formulation given by Eq. (4) is that once these atomic transition matrix elements are known and the dynamic structure factor has been experimentally determined at two or more momentum transfer values differing sufficiently to allow possible q dependence to be observed, Eq. (4) can be solved and $\rho_L(E)$ for the different L values extracted from the experimental data.

To apply Eq. (4), the experimental data needs to be carefully normalized as discussed in detail in **paper II**. The calculation of the matrix elements $M_L(q,E)$ has been implemented in an extension of a real space multiple scattering code FEFF8 [30,31], which also includes calculation of the x-ray Raman cross section. The method has been applied, for example, to the lithium K edge data from lithium metal in reference [32], besides the demonstration on the boron K edge in MgB_2 shown in **paper II**.

The scheme for determining $\rho_L(E)$ from the experimental XRS data is also extendable to doped and substituted systems as shown in **paper III**, where $\rho_L(E)$ have been determined from XRS data of boron K edge in an MgB_2 system, where some of the magnesium has been replaced with aluminum. The application of the method in **paper III** relies on the fact that as atomic like quantities, the matrix elements $M_L(q,E)$ are relatively stable against the aluminum substitution. Even between $M_L(q,E)$ calculated for pure MgB_2 and AlB_2, the maximum difference is only of the order of few percent. It is foreseeable that the same condition holds for a large variety of doped or substituted systems especially when the atomic numbers of the constituents do not change considerably or the dopant concentrations are low.

2.3 X-ray Emission

Photon induced x-ray emission stems from a scattering process described by the third term of the Eq. (1). In x-ray fluorescence emission, the incident radiation excites a core electron and the resulting core hole is filled by an electron from a higher energy orbital together with the emission of the fluorescence photon, whose energy is given by the energy difference of the involved core hole states. It is also possible to excite the initial core electron by e.g. high energy protons or electrons in addition to x-ray radiation. Depending on the involved core hole states, several fluorescence lines with varying energies and relative intensities can be observed [33,34]. Besides elemental analysis, where the atomic composition of a sample is determined from the energies of the excited fluorescence lines, fluorescence radiation is used in electronic structure studies by high energy resolution measurements of the emission line shape. In the hard x-ray regime the K fluorescence lines, which originate from a filling of a $1s$ core hole, have been applied especially to electronic structure studies of $3d$ transition metal systems.

In the following discussion on x-ray emission, the topic will be limited to the K fluorescence from $3d$ transition metals. Transition metals are especially interesting for the K emission studies as the interactions of the unfilled d shell with the core holes lead to a number of phenomena that provide an access to the electron configuration and interactions of the emitting ion.

For K fluorescence from $3d$ transition metals, the initial $1s$ hole can be radiatively filled by an electron from a $2p$ shell, in which case $K\alpha$ fluorescence is observed, or by a $3p$ electron, leading to $K\beta$ emission. The energies of the K fluorescence lines in $3d$ transition metals fall between 4 keV and 9 keV. It is also possible, that the core hole is filled by a valence electron giving rise to valence fluorescence (also referred to as $K\beta$ satellite lines) [35]. The valence fluorescence region has been, however, less utilized than the $K\alpha$ and $K\beta$ emission. When the incident photon energies are close the binding energy of the core electron[1], highly interesting resonance phenomena can be observed and used for electronic structure studies [35,36]. The following discussion will, however, concentrate on the case where the exciting x-rays have energies sufficiently high above the binding energy of the $1s$ core state, so that the more complicated resonance phenomena can be neglected.

The primary interest for K line emission studies has been the sensitivity of the emission line shape to the spin state of the emitting transition metal ion, especially in the case of $K\beta$ emission. Typical $K\beta$ emission spectrum from a $3d$ transition metal ion is divided into a main line $K\beta_{1,3}$ and a satellite line $K\beta$' due to the exchange interaction between the $3p$ core hole and the unfilled $3d$ shell in the final state of the emission process. The satellite structure is especially well illustrated in the manganese $K\beta$ emission spectrum from MnO, shown in Fig. 1. In a qualitative atomic picture of the emission process, the $K\beta_{1,3}$ main line originates from the final states with the $3d$ shell net spin parallel to the open $3p^5$ shell net spin, whereas transitions resulting in the $K\beta$' satellite come from the states, where in

---

[1] This regime is generally referred to as resonant inelastic x-ray scattering.

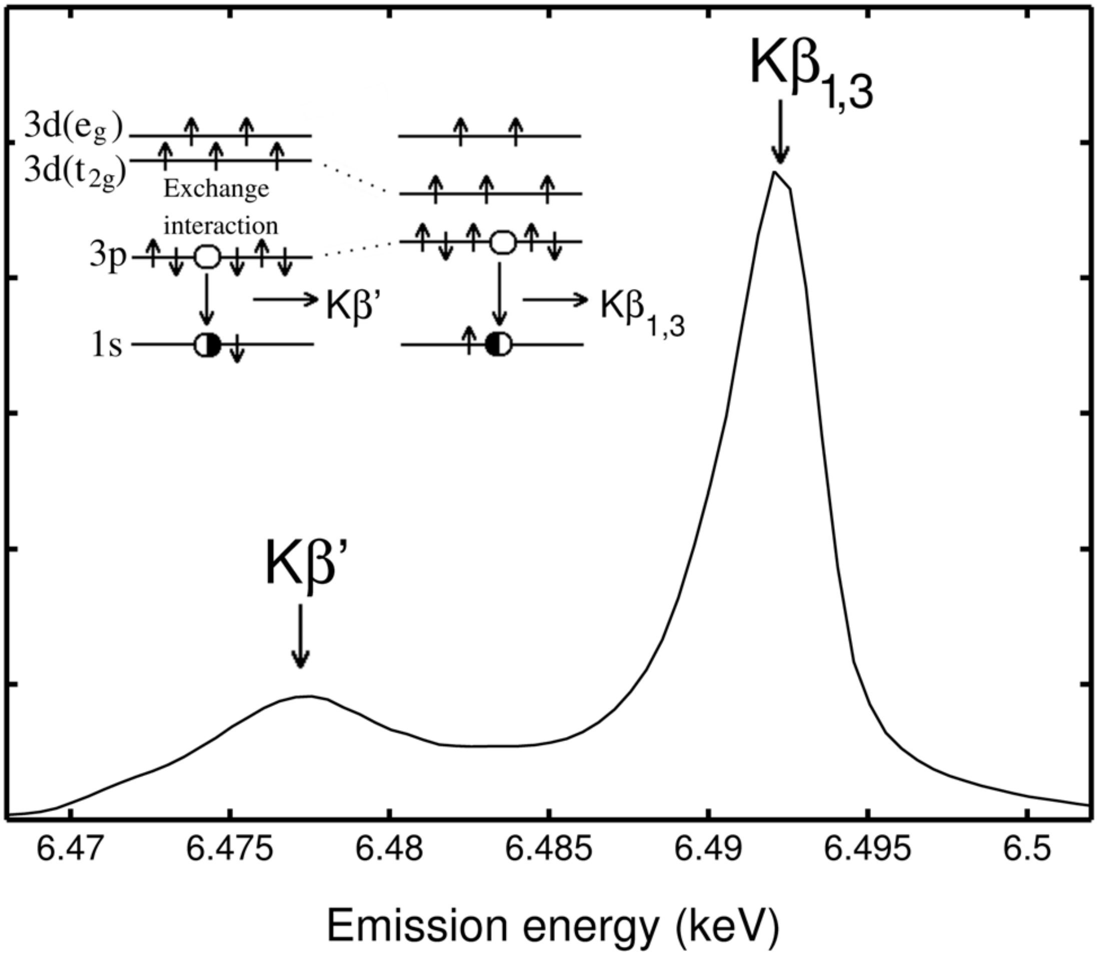

Fig. 1: A Mn $K\beta$ emission spectrum from MnO, taken from **paper V**. The main line $K\beta_{1,3}$ and the satellite line $K\beta$' are indicated in the figure by arrows. The inset shows a schematic diagram of the $K\beta$ process following the $1s$ excitation.

the final state the $3d$ shell net spin is reverse to the $3p^5$ shell net spin [37, 38]. The energy separation between the satellite and the main line in this picture is proportional to the strength of the exchange interaction and the satellite intensity to the net spin of the $3d$ shell.

Transition metal ions, for example, in insulating crystals are perturbed by the Coulombic field generated by the surrounding ions. In many oxides, transition metal ions are surrounded by six oxygen atoms arranged approximately octahedrally around the metal site. The negative effective charge of these oxygens creates an electric field that acts as a perturbation to the localized transition metal d electrons removing some of the degeneracy. The effect of this perturbation to the d electron states is dealt within ligand field multiplet theory [39], which has its roots in the work of Bethe from 1929 [40]. In case of octahedral arrangement of the coordinating oxygens the d states are split in energy into two sets, with the lower energy t_{2g} states accommodating 6 electrons and the higher energy

e_g states accommodating 4 electrons. Depending on the arrangement of the d electrons in these states, in case of 4 to 7 d electrons, one can have either a so-called high spin (HS) or a low spin (LS) ground state configuration. For example, in MnO the manganese atoms have 5 electrons in the $3d$ shell. These electrons can take either a LS configuration with $t_{2g}^5 e_g^0$ and $S = 1/2$ or a HS configuration with $t_{2g}^3 e_g^2$ and $S = 5/2$. In **papers IV-VI**, the ligand field picture of the transition metal ion d states is used to describe the observed spin state transitions. A common experimental arrangement has been to use $K\beta$ emission to extract the spin magnetic moment of the transition metal ion from a series of spectra measured under conditions where some variable, like the pressure or the temperature of the sample, has been changed to drive the studied system through an electronic phase transition. To analyze the $K\beta$ emission lineshape changes and to quantitatively relate the spectral shape to the spin magnetic moment of the emitting ion, a method based on the integrated absolute difference (IAD) spectra was proposed in **paper IV**. A number of different approaches have been utilized to follow the $3d$ shell net spin using the $K\beta$ emission line shape. The variation of the satellite intensity [41], the full spectral shape [42] or the main peak position [43, 44] have all been used as indicators of the spin magnetic moment. These various approaches have been reviewed in [45], where the authors found the IAD method to be the most reliable approach.

To briefly summarize the IAD approach, although the method is explained in detail in **paper IV**, the steps to analyze the spectra are (i) normalization to the same spectral area, (ii) aligning the spectra to the same center of mass value [44], (iii) subtracting a reference spectrum from all the analyzed spectra and integrating the absolute values of the difference [42], and (iv) converting the integral, or in other words the IAD value, to spin numbers by projecting the IAD scale on the spin scale given by the reference spectra. It is possible to use some of the spectra from the series under analysis as a reference [46] instead of a spectrum measured from another compound, if the spin number is known at e.g. some pressures or temperatures. This inner reference approach has been exploited in the **paper VI**, and reference compounds measured under similar experimental conditions in **paper IV**.

Other experimental techniques can also access the spin state of a transition metal ion besides x-ray emission spectroscopy. The change of a spin state can be seen, for example, in electronic and optical, vibrational, magnetic or structural properties but these usually do not provide a quantitative access to the spin state. Mössbauer spectroscopy is not directly sensitive to the spin but can access it through its sensitivity to the changes in the distribution of the d electrons. However, the technique is practically limited to iron compounds and requires special sample preparation. Magnetic susceptibility generally gives direct information on all the magnetic ions in a system and impurity contributions are in some cases difficult to separate from the transition metal ion signal. The pre-edge region of the transition metal K edge absorption spectrum, where part of the intensity is due to transitions to the empty $3d$ states, is also, in principle, sensitive to the spin state [47]. The pre-edge region was studied also in **paper IV** of this thesis, but generally the region is weak in intensity and poorly resolved. Soft x-ray absorption spectroscopy [48–50] in the metal $L_{2,3}$ edges is also a powerful technique in determining the spin state. However, as a soft x-ray technique with the absorption edge energies below 1 keV for $3d$ metals, the method is not compatible e.g. with diamond anvil cell techniques.

3 Computational Methods

Many advancements in condensed matter physics during the past decades can be attributed to improved computational methods for determining the electronic structure, made possible by a notable extent of the computational power of modern computers. For x-ray spectroscopies, advances in understanding the physics of the excited states in addition to the ground state electronic structure has been a key development [51]. Some of the various computational approaches have been reviewed in reference [52], for example. In the following, brief introductions to the main computational techniques utilized in this thesis i.e. to the real space multiple scattering calculations and to the cluster multiplet approach will be given.

3.1 Multiple Scattering Formalism

The real space multiple scattering approach originates from the early theoretical models used for describing the origin of the oscillating intensity modulations in x-ray absorption spectra observed above the absorption edges [53]. The basic idea of the real space multiple scattering approach is to follow the interactions and scattering of the excited core-electron wave from the surrounding atoms. The following discussion will examine how this approach is implemented in a real space multiple scattering code FEFF [30, 31] which has been recently extended to include calculations of the XRS cross-section[2].

The FEFF code employs a Green function approach to formulate the scattering cross section, or in case of XRS, the dynamic structure factor. The Green's function approach reformulates the dynamic structure factor as $S(\mathbf{q},\omega) = -1/\pi \,\mathrm{Im}\, \langle I|e^{-i\mathbf{q}\cdot\mathbf{r}'} PG(\mathbf{r},\mathbf{r}';E)Pe^{-\mathbf{q}\cdot\mathbf{r}'}|I\rangle$, where E is the photoelectron energy, $E = \omega + E_I$, and P is a projection operator casting the Green's function or the propagator G to the unoccupied states of the initial state Hamiltonian [54]. The propagator G contains all the possible ways the photoelectron can interact with the system and is related to the final state Hamiltonian H' of the system through $G = [E - H' + i\tau]^{-1}$, where τ is the core hole lifetime.

The final state Hamiltonian $H' = p^2/2m + V_C' + \Sigma\,(E)$, where p is the momentum operator and m is the electron mass, is a sum of the kinetic part given by the first term and the total electron potential given by the last two terms. The potential consists of a Coulombic part V_C' and an electron self-energy $\Sigma(E)$, analogous to the exchange correlation

---

[2] A number of other code packages employing real space multiple scattering approach exists. See, for example, the listing at the www-page http://xafs.org/Software.

potential of a ground state calculation [55]. A number of different approximations are available in the FEFF code for $\Sigma(E)$ (see e.g. [53]). For x-ray Raman calculations, the choice for the energy dependent self-energy has been the local density approximation of Hedin and Lundqvist [56]. The Hedin-Lundqvist self-energy is based on a uniform electron gas model within a plasmon pole approximation. The Hedin-Lundqvist model is generally sufficient for the moderate photoelectron energies, which are of interest from the point of view of near edge XRS experiments [53].

The Coulombic part of the potential in FEFF is constructed using the muffin-tin approximation. The charge densities within the muffin tins are obtained from a Dirac-Fock-Desclaux code [57] and the overlapping muffin-tin approach [58] is used to construct the initial charge density. The real space construction of the potential makes the code highly flexible, allowing calculations for molecules and systems that lack translational symmetry. The scattering potential is self-consistently calculated by iterating the total electron density, potential and Fermi energy. The potential is first calculated from the initial charge density by adding a local exchange. With the new potential, new charge density is calculated. The potential and density are iterated until convergence is reached. In the full multiple scattering solution the propagator $G = (1 - G^0 t)^{-1} G^0$, where G^0 propagator describes electron propagation between two points in the real space and t the photoelectron scattering from neighboring atom, is solved exactly by matrix algebra. However, the full multiple scattering calculation is limited in cluster size (typically to a few hundred atoms cluster) and also in energy only to the near edge region roughly a hundred eV over the absorption edge energy. For extended energy regions, a path expansion of the propagator G is used to speed up the calculations [31].

All the FEFF calculations shown in **papers I-IV** utilize the self-consistent potential calculation and full multiple scattering approach. Besides work presented in this thesis, the XRS cross section calculations implemented in FEFF have been recently used for studies of L edges in silicon, magnesium and sodium [59] and of carbon K edges in polyfluorene samples [60].

3.2 Cluster Multiplet Calculations

The cluster multiplet (also called charge transfer multiplet) approach for the electronic structure calculations of strongly correlated d and f electron systems is based on the Anderson impurity model [61]. The cluster multiplet approach was developed during 1980's by the groups of Kotani [62], Fujimori and Minami [63], Gunnarsson and Schönhammer [64] and Sawatzky and co-workers [65–67] to explain various core level spectroscopies including x-ray photoemission, bremmsstrahlung isochromat spectroscopy and $L_{2,3}$ edge x-ray absorption spectra of especially nickel and copper oxides and halides. Several reviews on cluster multiplet calculations and theory including discussion on the related experimental work are available [36, 49, 50, 68–70] and only a short description of the basic principles of the approach is given here. The following presentation is focused on the $3d$ transition metal oxide compounds and a formulation will be made for calculating the x-ray induced K fluorescence emission spectra from these systems.

The starting point of the Anderson impurity model is the fact that the $3d$ states are generally considerably localized in space in strongly correlated transition metal systems. In strongly correlated electron systems, one-electron theories including the local density approximation in density functional theory fail to properly describe the ground state electronic properties, like the band gap, correctly. In $3d$ transition metal systems, the strong Coulomb interaction between the d electrons effectively localizes these to a single transition metal ion site leading to an insulating ground state even though the unfilled d shell would generally create a conductor. Theoretical challenges posed by these systems are very much deriving from the problem that the electronic structure is neither described by one-electron theories nor it is completely ionic: both the localized and itinerant interactions need to be considered in the theoretical models of strongly correlated electron systems on equal footing.

The interaction of the $3d$ electrons with the occupied valence band is considered to be a more dominant interatomic interaction, while the coupling to the empty conduction band is less important [50]. The conduction band is typically at higher binding energies than the valence band leading to a bigger energy gap between the $3d$ electrons and the conduction band than between the $3d$ electrons and the valence band. For oxides, the valence band is formed by the filled oxygen 2p states (the transition metal $4s$ electrons fill the oxygen $2p$ band).

The Anderson impurity model based Hamiltonian H_I takes into account a single transition metal ion and all oxygen ions, whose $2p$ states form the valence band. A core electron of the transition metal ion is excited in the x-ray emission process. The Hamiltonian, written in the second quantized form using the annihilation $a^\dagger$ and creation operators a, is given by [36, 70]

$$\begin{aligned} H_I \;=\; & \sum_{\Gamma,\sigma} \varepsilon_{d\Gamma} a^\dagger_{d\Gamma\sigma} a_{d\Gamma\sigma} + \sum_{m,\sigma} \varepsilon_p a^\dagger_{pm\sigma} a_{pm\sigma} + \sum_{\sigma} \epsilon_s a^\dagger_{s,\sigma} a_\sigma + \sum_{\Gamma,k,\sigma} \varepsilon_{\Gamma k} a^\dagger_{\Gamma k\sigma} a_{\Gamma k\sigma} \\ & + \sum_{\Gamma,k,\sigma} V\left(\Gamma k\right)\left(a^\dagger_{d\Gamma\sigma} a_{\Gamma k\sigma} + a^\dagger_{\Gamma k\sigma} a_{d\Gamma\sigma}\right) - U_{dd} \sum_{(\Gamma,\sigma)\neq(\Gamma',\sigma')} \left(a^\dagger_{d\Gamma\sigma} a_{d\Gamma\sigma} a^\dagger_{d\Gamma'\sigma'} a_{d\Gamma'\sigma'}\right) \\ & - U_{dc}\left(p\right) \sum_{\Gamma,m,\sigma,\sigma'} a^\dagger_{d\Gamma\sigma} a_{d\Gamma\sigma}\left(1 - a^\dagger_{pm\sigma} a_{pm\sigma}\right) - U_{dc}\left(s\right) \sum_{\Gamma,\sigma,\sigma'} a^\dagger_{d\Gamma\sigma} a_{d\Gamma\sigma}\left(1 - a^\dagger_{s\sigma} a_{s\sigma}\right) \\ & + H_{multiplet}. \end{aligned} \tag{5}$$

The first three terms on the right hand side of the Eq. (5) represent the transition metal ion $3d$, p and s symmetry shells, with energies $\varepsilon_{d\Gamma}$, ε_p and ε_s, respectively. Only the s and p shells involved in the x-ray emission process are considered. The fourth term is the occupied valence band formed by the oxygen $2p$ electrons with energy $\varepsilon_{\Gamma k}$, where the summation over the index k is due to the energy spread of the band. Generally, the valence band is discretized in the calculation, with N discrete k values spread over a bandwidth W.

If the summation over the k values is not considered, the valence band is reduced to the $2p$ states of the neighboring oxygen sites. The model including only the neighboring oxygen $2p$ orbitals is then generally referred to as a cluster model (i.e. the cluster model Hamiltonian corresponds to the Anderson impurity model Hamiltonian in the limit of vanishing W).

The splitting of the $3d$ band due to the electrostatic field of the neighboring oxygen ions (the ligand field) acting on the $3d$ electrons is accounted for by the summation over the irreducible representations Γ of the local symmetry group of the transition metal ion [39]. The energies of these different irreducible representations are included in $\varepsilon_{d\Gamma}$. The same local symmetry as for $3d$ electrons is assumed for the valence band.

The hybridization is given by the fifth term, where $V(\Gamma k)$ gives the strength of the interaction. This term is responsible for the charge transfer between the valence and the $3d$ band. The strength of the spherically averaged Coulomb interaction between the $3d$ electrons is given by the U_{dd} in the sixth term. The spherically averaged Coulomb interaction strength between the $3d$ electrons and the s or p shell hole in the intermediate or the final state is given by $U_{dc}(s)$ and $U_{dc}(p)$, respectively, in the seventh and eight terms. The $H_{multiplet}$ includes the intra-atomic multiplet couplings originating from interaction between the $3d$ electrons and those between the p and s states and $3d$ states. In addition, the spin-orbit interactions are contained in the $H_{multiplet}$ term.

The ground state configuration set for the Hamiltonian H_I is a linear combination of $3d^n, 3d^{n+1}\underline{L}, 3d^{n+2}\underline{L}^2, \cdots$ configurations, where $\underline{L}$ denotes a hole in the valence band. The number of possible configurations is to some extent set by computational limits. Especially for systems with half-filled d shells, the number of possible multiplet terms becomes a restrictive factor and usually the calculations are performed with a maximum of three configurations. Often, the fourth configuration would also have a very high energy and practically a zero weight in the ground state.

The calculation of a Kβ emission involves core hole states, with a $1s$ core hole in the intermediate and a $3p$ core hole in the final state of the emission process. Within the three configuration basis set the emission process would go through $3d^n + 3d^{n+1}\underline{L} + 3d^{n+2}\underline{L}^2 \rightarrow 1s^1 3d^n + 1s^1 3d^{n+1}\underline{L} + 1s^1 3d^{n+2}\underline{L}^2 \rightarrow 3p^5 3d^n + 3p^5 3d^{n+1}\underline{L} + 3p^5 3d^{n+2}\underline{L}^2$ configurations in the initial, intermediate and final states. These different configurations together with the relative energies are shown in Fig. 2.

In the actual calculation, the multiplet terms contained in $H_{multiplet}$ are first obtained using an atomic Hartree-Fock calculation [71]. The atomic values for the spin-orbit couplings are used, where as the Slater integrals are usually reduced to account for intra-atomic configuration interactions not included in the $H_{multiplet}$, which effectively reduce the values of the Slater integrals [49]. The effect of the local symmetry is then considered using the group theoretical approach developed by Butler [72]. The Hamiltonian given by Eq. (5) is finally diagonalized to obtain the state energies.

The $K\beta$ emission intensity $I(\omega_2)$ at the emitted photon energy ω_2 is calculated using a formulation taking into account the intermediate $1s$ and final state $3p$ core hole lifetimes

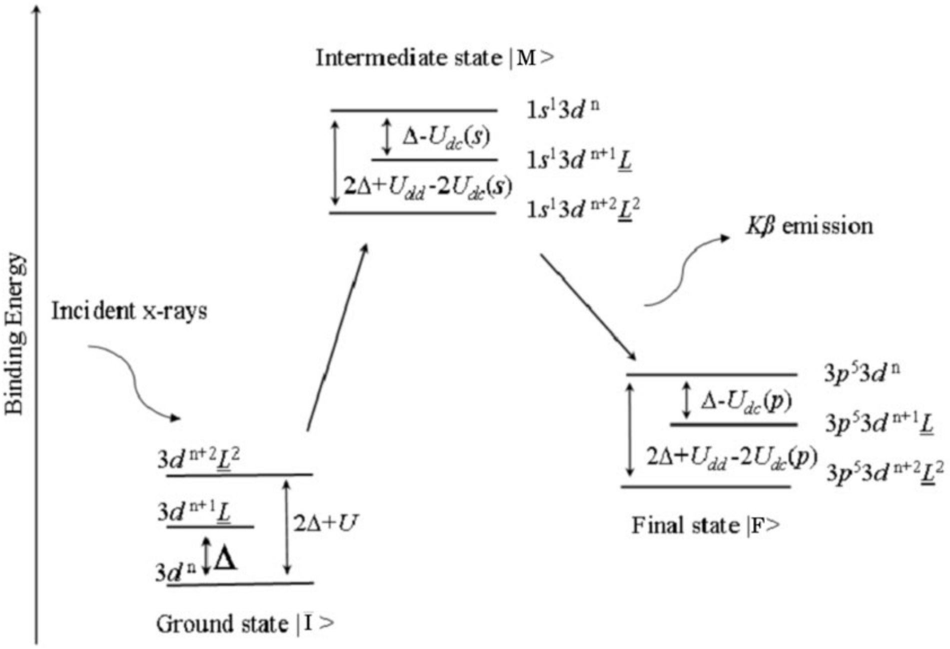

Fig. 2: Scheme of the different configurations in the initial, intermediate and final state of x-ray excited $K\beta$ emission. The relative energy differences of the configurations are indicated in the figure (see text for definitions of Δ, U_{dd}, $U_{dc}(s)$, $U_{dc}(p)$, and $\underline{L}$). The excited $1s$ photoelectron is assumed to be in the far continuum and is not included in the intermediate and final state configurations. The relative energy positions of the different configurations depend on the values of Δ, U_{dd}, $U_{dc}(s)$ and $U_{dc}(p)$.

Γ_K and Γ_M,

$$\begin{aligned} I(\omega_2) \quad \propto \quad & \int d\epsilon \sum_F \left| \sum_M \frac{\langle F|T_2|M\rangle\langle M|T_1|I\rangle}{E_I+\omega_1-\epsilon-E_M-i\Gamma_K} \right|^2 \\ & \times \frac{\Gamma_M/\pi}{(E_I+\omega_1-\epsilon-E_F-\omega_2)^2+\Gamma_M^2}, \end{aligned} \tag{6}$$

where again $|I\rangle$, $|M\rangle$ and $|F\rangle$ are the initial, intermediate and final states with energies E_I, E_M and E_F, respectively. The T_i are dipole transition operators responsible for the creation of the $1s$ core hole and for the transition of the core hole from $1s$ to $3p$ level with the emission of a fluorescence photon. The incident photon energy is given by ω_1. The integral is taken over the photoelectron energies ϵ. The integration produces a prefactor before the matrix elements and make the emission lineshape independent of the incident energy ω_1 [68]. Also, the summation over the intermediate states $|M\rangle$ can be neglected as the effect of coherence is usually small for K emission. The lifetimes (full width at half maximum values) for the $1s$ hole states range, for example, between 1.1 eV for manganese to 1.5 eV for copper. For Kβ emission one has to also take into account the fact that the lifetimes of the $3p$ core hole states are not constant as the probability of the non-radiative primary decay channel for the $3p$ core hole state is strongly dependent on the LS value of the particular state [73]. For calculating the manganese $K\beta$ emission, for example, a linear lifetime dependence $\Gamma_M = -0.1(\omega - \omega^0)$, with ω^0 denoting the main emission line energy position, has been found to be a sufficient approximation to produce a good correspondence with the experiment [74, 75]. This linear final state lifetime model is also used in **papers IV-VI**.

The cluster multiplet approach requires that a number of parameters are determined by fitting the calculated spectra to the experiment. The parameters to be determined in the case of the Hamiltonian given by Eq.(5) are the hybridization strength $V(\Gamma)$, which is usually averaged over the k values, the Coulomb interaction strengths U_{dd} and U_{dc}, and the charge transfer energy Δ, given by

$$\Delta = E\left(3d^{n+1}\underline{L}\right) - E\left(3d^{n}\right), \tag{7}$$

where $E(3d^n)$ is the energy averaged over the multiplet term of the $3d^n$ configuration. Also, the strength of the crystal field interaction has to be set in the calculation. Generally, the values of some of the terms are dependent on the involved configuration. An analysis of the crystal field interaction strength suggests that generally for core hole states the crystal field values are about 10-20% smaller [76]. Also, the hybridization parameter value is reduced for the core hole state [77]. Both reduction effects stem from the fact that the core hole effectively contracts the $3d$ wave function leading to a reduced overlap with the neighboring atoms. Between manganese and copper, charge transfer energies generally varies between 3 eV and 10 eV in divalent compounds and the U_{dd} Coulomb interaction generally between 6 eV and 10 eV [3].

The cluster multiplet approach is used for the analysis of the experimental data in **papers IV-VI** of this thesis. In all these papers x-ray $K\beta$ emission lineshapes from transition metal oxides are analyzed using the method detailed above and the observed spin transitions are explained by the reordering of the $3d$ electrons in the crystal field split $3d$ states. In **paper IV**, the cluster multiplet approach is also used to analyze the quadrupolar components of the cobalt K edge x-ray absorption spectra.

4 Experiments

The experimental work presented in this thesis was done at the European Synchrotron Radiation Facility (ESRF) at the beamline ID16. The beamline is designed for inelastic x-ray scattering experiments both in the eV energy resolution range for electronic excitation studies and in the meV energy resolution range for phonon studies. The beamline houses eV resolution spectrometers for both x-ray Raman and x-ray emission studies. Besides

---

[3] The parameters U_{dd}, Δ and W can be used to classify the different transition metal compounds according to the type of the charge gap within the Zaanen-Sawatzky-Allen framework [66].

the beamline setup, different sample environments have been crucial for the success of the experiments. Especially the high pressures generated using a diamond anvil cell pose several experimental challenges beyond the measurement of the x-ray spectra at the beamline.

4.1 Beamline ID16 at ESRF

The radiation on the beamline ID16 is produced by three consecutive undulators. The setup of the beamline after the undulators in shown in Fig. 3. The main optical components for eV resolution studies before the sample stage are a monochromator and a focusing mirror. The energy of the incident radiation is chosen using a double crystal monochromator utilizing the Si(111) reflection. The monochromator allows the continuous changing of the incident energy with the beam position staying sufficiently stable at the sample position. An optional channel-cut monochromator can be inserted into the beam to further narrow the energy bandwidth of the transmitted radiation. The x-rays are focused to the sample position by a rhodium coated toroidal mirror, which provided for the work presented in this thesis a minimum spot size of roughly $150(H) \times 100(V)\mu\mathrm{m}^2$.

A pin diode detector is used to measure the intensity of the scattered radiation from a Kapton foil placed after the focusing mirror to monitor the intensity of the incident radiation. Additional intensity monitors are also used, the exact configuration varying between different experiments. Usually, one secondary intensity monitor is employed to measure the scattering from a short air path or scattering from the actual sample. The scattered radiation from the sample was analyzed in all the experiments presented in this thesis using a crystal spectrometer operating in a Rowland circle geometry. The spectrometer Rowland circle had a radius of 1 m. The scattered radiation was finally detected by a Si diode detector. The ID16 spectrometer is equipped with a single analyzer crystal. Recently, crystal spectrometers with several analyzer crystals have been commissioned. The motivation for this type of setup is to increase the solid angle in which the scattered radiation is collected or to measure spectra at several different momentum transfers simultaneously. These designs utilize several crystals focused on a single detector [78], while some realizations employ several detectors [79] or a 2D detector [80] to separately record the contributions from each individual crystal.

In the x-ray Raman experiments, the energy transfer was controlled by tuning the incident energy and analyzing the intensity of the scattered radiation at a fixed analyzer energy. In this so called inverse energy scan mode the analyzer Bragg angle stays fixed, so that nearly backscattering geometry can be used in order to minimize the source size contributions to the analyzer energy resolution. Constant Bragg angle also eliminates the need for a detector translation stage. The inverse energy scan mode, however, requires careful incident intensity monitoring. The momentum transfer in an x-ray Raman experiment is controlled by the scattering angle. The experimental setup limits the scattering angles to values roughly below 165°. In the x-ray Raman experiments presented in **papers I** and **III**, the scattered radiation was analyzed in horizontal scattering geometry using

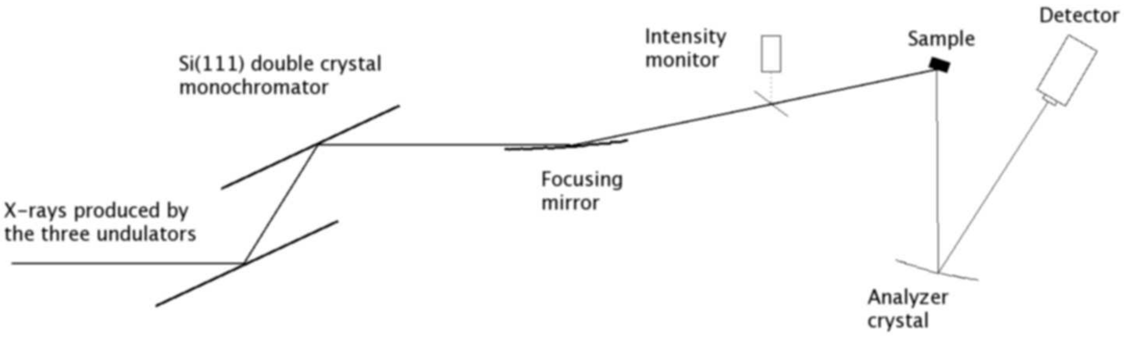

Fig. 3: The layout of the experimental setup at the beamline ID16.

Si(444) and Si(555) reflections with the corresponding photon energies at about 8 keV and 10 keV, respectively. With this choice of analyzers, the maximum momentum transfer values have been about 9 Å^{-1}. The total energy resolutions reached with this setup have been 1.1 eV for Si(444) and 1.5 eV for Si(555) reflections without the additional channel-cut monochromator.

In practice, the usable momentum transfer range in an x-ray Raman experiment is limited, besides constraints placed by the spectrometer, by the background contribution stemming from the inelastic scattering from the valence and core electrons at higher orbitals. The maximum of this inelastic scattering background moves towards higher energy transfers as the momentum transfer is increased. At some momentum transfer values, the maximum of the inelastic background can coincide with the edge position, making the removal of the background contribution more difficult.

The polarization dependence of the non-resonant inelastic cross section entering through the Thompson cross section has to be taken into account as the x-rays produced by the undulator source are linearly polarized with the polarization in the horizontal plane. In horizontal scattering geometry with the scattering angles close to 90° the polarization dependence leads to a strong suppression of the inelastic scattering signal. This polarization dependence of the non-resonant inelastic scattering can be, on the other hand, used in emission experiments to suppress the background by recording the emission at 90° scattering angle.

In x-ray emission experiments the spectrometer setup is more complicated as the Bragg angle of the analyzer crystal has to be scanned and the detector needs to follow the reflection from the analyzer crystal. If a strict Rowland circle geometry is to be maintained, the distance between the analyzer crystal and the detector would change as the Bragg angle is scanned, complicating the vacuum tank construction between the sample, analyzer and detector. The spectrometer utilized for the resonant experiments presented in **papers IV-VI** used a linear translation stage that moved the detector in a direction perpendicular to the detector-analyzer direction, while simultaneously rotating the detector towards the analyzer crystal. The experiments in **papers IV-VI** were done in a horizontal scattering geometry. In **paper VI** the analyzer scattering plane was vertical. The main advantage of this vertical geometry is that small sample position movements along the incident x-ray beam do not change the analyzer energy calibration and small shifts in the emission line energy position could be followed reliably.

Each XRS and x-ray emission spectrum were measured several times and the accumulated spectra were summed up. The total accumulation times needed to obtain a sufficient statistical accuracy in the summed spectrum ranged from about 30 minutes for $K\beta$ emission spectra to 12 hours for x-ray Raman experiments. The repeated scanning of the same spectrum is crucial in synchrotron experiments especially when the total measurement time for one spectrum is in the range of several hours. As the ring current at the ESRF storage ring decays as a function of time, the heat load on the optical components change, possibly resulting in small shifts in the beam position and in a drop of the photon flux at the sample position. The complications of decaying ring current can be circumvented by constantly injecting electrons into the storage ring. This filling mode has been adopted at the Advanced Photon Source (APS) and SPring-8 synchrotron radiation source, for example. In addition to issues related to the storage ring operations, the mechanical stability of the optical components during the repeated scanning has to be monitored and before summing up, the spectra are routinely checked for consistency to verify the proper alignment and working of the beamline optics.

The experimental work presented in **paper IV** has required a careful controlling of the sample temperature and in **papers IV-VI** the ability to subject the samples to static pressures in the 100 GPa range. Sample cooling in **paper IV** has been achieved using a standard closed-cycle helium cryostat, which is equipped with x-ray transparent windows. To reach temperatures above the room temperature the sample was placed on a resistive heater. Both in the low and high temperature setups the sample was in vacuum. The high pressure sample environment is described in detail in the next section.

4.2 The High Pressure Diamond Anvil Cell

Papers IV-VI describe experiments where static pressures up to 140 GPa are generated on the sample using diamond anvil cells. Several different diamond anvil cell designs exists [81, 82] and the following discussion will mostly deal with the common Mao-Bell type cells [83], although most of the details are independent of the exact cell design. Fig. 4 shows a schematic picture of a diamond anvil cell together with a picture of a gas membrane driven diamond anvil cell. In the diamond anvil cell, the sample is placed between the flat, parallel faces of two opposed diamond tips. The sample is held in place by a metallic ring called the gasket, and pressure is generated by pushing the two diamonds, sitting on backing plates, together. Force is applied to the diamonds through the backing plates either by a set of screws or by a metallic gas operated membrane. The generation of high pressures in the diamond anvil cells is based on minimizing the sample and diamond tip

Fig. 4: The left panel shows a schematic picture of a diamond anvil cell. The top and bottom diamonds are supported by backing plates not shown in the drawing. The middle panel shows an assembled gas membrane driven diamond anvil cell. The diamond anvil is visible in the middle of the circular support structure in the right panel.

surface area (as pressure $P = force/area$). Usually, the diamond tip diameter has to be in the 100 μm range for work at 10-100 GPa range. The upper pressure limit is set by the physical strength of the diamond anvils and the highest pressures reached have been above 350 GPa [84].

The diamond cell loading begins by ensuring the parallelism and overlapping of the diamond tips. A gasket is pre-indented with the diamonds and a hole, which will act as a sample cavity, is drilled to the gasket. The gasket material varies according to the needs of the experiment, in **papers IV** and **VI** rhenium gaskets were utilized, whereas in **paper V**, x-ray transparent beryllium gaskets were used. The initial rhenium gasket thicknesses in **paper VI** were about 200 μm and the gaskets were pre-indented to about 20-30μm thickness, whereas with beryllium gaskets used in **paper V**, an initial thickness of about 1 mm was used and the gasket was pre-indented to about 100 μm thickness. The sample hole diameter is taken to be about one third of the diamond tip (culet) diameter for non-beveled diamonds. With beveled diamonds, the hole is usually slightly bigger, of about half of the diameter of the diamond flat. The function of the gasket, besides confining the sample, is also to support the diamond anvils and to increase the maximum achievable pressure in the cell [85].

The sample and a pressure gauge, alongside with a possible pressure transmitting medium to achieve a hydrostatic pressure, is then loaded in to the gasket hole and the diamonds are pressed together. The choice of the pressure medium depends on the required pressure range as many liquids solidify at relatively modest pressures [86]. In **paper IV**, for example, a mixture of methanol-ethanol (4:1) was used as a pressure medium. The cell can be prepared and loaded also in a high pressure gas environment. After the cell is closed, the gas in the sample chamber will act as a pressure medium. High gas pressures are used to maximize the amount of gas in the sample chamber. Gas loading technique was used in **paper VI**.

The pressure inside the diamond anvil cell can be determined using a ruby fluorescence method [87]. A small ruby chip of few μm in diameter is placed in the sample chamber and fluorescence light is excited typically using a laser light. The ruby R_1 and R_2 doublet lines, which at ambient pressure are at 6927 Å and 6942 Å respectively, shift to higher wavelengths with increasing pressure with an almost linear dependence of the wavelength on the pressure. Ruby lines are generally difficult to use above 100 GPa pressures and alternative pressure calibrants generally need to be used [88].

With rhenium gaskets, the x-ray emission experiments are performed through the diamond anvils. With beryllium gaskets, it is possible to use a geometry where the scattered radiation is detected through the gasket [89]. For high pressure x-ray emission studies shown in **papers IV-VI**, incident photon energies between 12 keV and 15 keV were used to excite the fluorescence, a compromise between the absorption of the incident radiation in the diamond anvil and the x-ray emission cross section.

Future developments for generating high pressures will involve larger sample volumes [90] and improved techniques to heat samples inside the cell in the several 1000 K range using laser heating techniques [91], for example, to better simulate conditions at Earth's mantle and core region. X-ray emission experiments with high quality perforated anvils [92] are also a very promising development, allowing possibly access to the early $3d$ transition metals using K shell emission spectroscopies.

5 Summary of the Papers

The six individual research papers presented in this thesis fall into two adjacent lines of research. The first three papers present x-ray Raman scattering results on the electronic structure of a novel superconducting material MgB_2. The last three papers deal with x-ray emission studies on pressure- and temperature induced magnetic transitions in transition metal oxides. Besides the slightly differing experimental techniques, the studied systems are also different from the theoretical point of view. The electronic structure of the metallic MgB_2 can be understood within first principles band structure calculations, whereas the phenomena in strongly correlated transition metal oxides are approached using the cluster multiplet model.

The first three papers discuss XRS experiments on pure and aluminum substituted MgB_2. The experimental results are compared with theoretical calculations of the XRS spectra and the electronic structure. Two of the papers demonstrate the application of a decomposition scheme for extracting the final state density of electron states from the XRS data and show how this method can be applied to doped and substituted systems to follow electron or hole doping induced changes in the empty electron states.

In **paper I**, XRS spectroscopy is used to study the electronic structure of MgB_2 superconductor. MgB_2 is a metallic superconductor with a critical temperature of superconductivity $T_C \approx 39K$ [93], which is the highest known T_C for a conventional, BCS type superconductor [94]. High density of empty electron states at the Fermi level, provided by

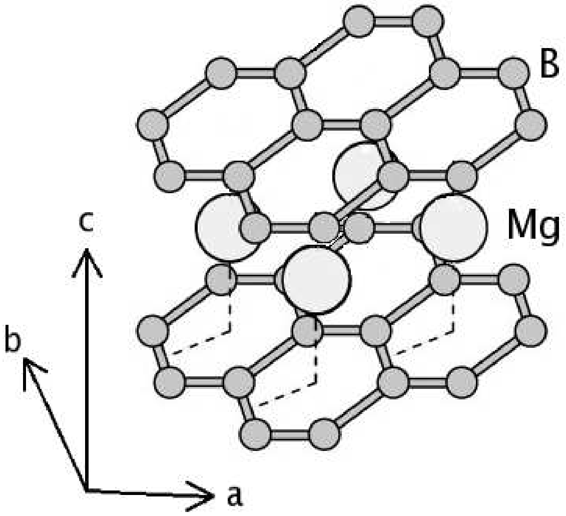

Fig. 5: Crystal structure of MgB_2. Boron atoms (dark form honeycomb planes and magnesium atoms occupy the centers of the hexagons in between the boron planes.

the boron σ and π bands, is an important feature of the electronic structure contributing to the high T_c in MgB_2. The σ band derives from the hybridized boron sp_xp_y orbitals, while the π band is formed by the p_z orbitals. These two bands have different electron-phonon coupling strengths [93, 95–97] leading to a realization of two-band superconductivity [98] although MgB_2 still has only one transition temperature due to weak interband phonon scattering between the σ and π bands [97].

The MgB_2 crystal structure, shown in Fig. 5, consists of alternating layers of magnesium and boron atoms. The quasi 2D σ band resides within the boon sheets and couples strongly to boron-boron E_{2g} bond oscillations, leading to the larger superconducting energy gap [99, 100]. The smaller gap originates from the π band with a weaker electron-phonon coupling strength. In **paper I**, the physically interesting σ and π bands were probed using XRS at the boron K edge on a single crystal MgB_2 sample. The XRS cross section dependence on the direction of the $\mathbf{q}$ vector relative to the crystal orientation was used to separate the contributions from the boron σ and π states. Using the dependence of the XRS cross section on the magnitude of the momentum transfer, a vanishing density of s symmetry states near the Fermi level was also demonstrated. The observed density of both σ and π band states and a vanishing density of the empty s symmetry states near the threshold highlight the crucial role of especially the σ band states in setting the superconducting properties of MgB_2. The theoretical interpretation of the XRS spectra was largely based on a Bethe-Salpeter equation based first principles calculations of the XRS cross section [101, 102].

Paper II examines the recently developed decomposition scheme for extracting the final state density of electron states from the XRS data and the method is applied to the experimental results of **paper I**. **Paper II** details and critically examines the practical steps needed to apply the scheme to experimental data. The results confirm the conclusions drawn in **paper I**. The computational results presented in this paper are based on the FEFF code version developed for XRS cross section calculations [30, 31].

Paper III continues the work of MgB_2 system and demonstrates how to apply the decomposition scheme discussed in **paper II** to doped and substituted systems. The aluminum substitution for magnesium dopes the system with electrons that fill the boron σ and π band states and lowers the critical temperature of superconductivity, for example, in the present sample to 28.2 K [103–106]. Besides band filling atomic substitutions change the phonon scattering rates, and the exact roles of band filling and phonon spectrum changes behind lowering the T_C in the substituted systems are still debated [103–108].**Paper III** presents XRS spectra at the boron K edge in $Mg_{0.83}Al_{0.17}B_2$ single crystal sample and extracts the boron final state density of electron states $\rho_L(E)$ from the experimental data for comparison with the boron $\rho_L(E)$ from pure MgB_2. Compared to the density of states of pure MgB_2, the σ band density of states in aluminum substituted sample decreased at the Fermi level by about one quarter, while the π band hole count was relatively stable. These results shed light on the role of the band filling in lowering the T_c in the substituted sample. In summary, the work presented in **papers I-III** fully utilizes the momentum transfer dependence of XRS in electronic structure studies of MgB_2 and shifts XRS spectroscopy to a more quantitatively level.

Paper IV, first of the three emission spectroscopy papers, examines temperature and pressure induced spin state transitions in $LaCoO_3$. The motivation for the study was the long standing question concerning the nature of the Co spin states at various temperatures and pressures. Traditionally, these transitions have been analyzed in terms of cobalt HS $t_{2g}^4 e_g^2$ $(s = 2)$ and LS $t_{2g}^4 e_g^2$ $(s = 0)$ configurations. A proposed formation of an intermediate spin (IS) state with $t_{2g}^5 e_g^1$ $(s = 1)$ configuration at the first thermally induced spin state transition has contributed considerably to the recent interest in these compounds [109] and called for new experimental results on the cobalt magnetic moment at various temperatures and pressures.

In **paper IV**, the temperature dependent evolution of the cobalt $K\beta$ emission spectra from $LaCoO_3$ together with the cobalt K edge XAS in a temperature range of 17 K to 913 K was measured. The cobalt $K\beta$ emission spectra as a function of pressure from ambient to 10 GPa pressure was also recorded. The $K\beta$ emission spectra and the pre-edge features of the cobalt K edge absorption spectra were compared to cluster multiplet calculations and the real space multiple scattering code FEFF was used to analyze the cobalt K edge x-ray absorption spectra over a more extended energy range. In addition, it was proposed that the integrated absolute difference of the emission spectra (the IAD line shape analysis) could be used to quantitatively extract the spin magnetic moment from the x-ray emission data. The first thermal spin transition at around 90 K was interpreted as a transition of the cobalt ion ground state from a low temperature LS state to a high temperature IS state with a continuous redistribution of the $3d$ electrons between t_{2g} and e_g levels. The evolution of the emission line shape with increasing pressure also confirmed that the ground state was driven back to LS state between 4 GPa and 7 GPa pressures at room temperature.

Paper V describes high pressure x-ray emission experiments on transition metal monoxides. The possibility to use pressure to change lattice distances and electron densities in strongly correlated compounds is a very interesting prospect to gain further understanding on the basic physical phenomena in these systems. With increasing electron density the electron interactions and localization is modified, while the constituents of the system stay constant, unlike when these properties are modified by doping [110]. In **paper V** these phenomena were studied in transition metal monoxides MnO, CoO, FeO and NiO using Kβ emission spectroscopy. A detailed description of the experiments is given in [89] and the **paper V** concentrates on the theoretical analysis of the pressure induced changes in the electronic structure using cluster multiplet calculations. The magnetism is modified in the 60 GPa to 140 GPa pressure range in all the monoxides except NiO. Within the crystal field model, these transitions can be described as HS to LS transitions. Hybridization and ligand bandwidth are found to increase with pressure, alongside with the crystal field, whereas the charge transfer and *dd* correlation energies are not strongly affected by pressure, a finding supported by a resonant inelastic x-ray scattering experiment at the nickel K edge in NiO [111]. The calculations also indicate that the high pressure LS phase is stabilized by the increasing ligand bandwidth in addition to changes in the crystal field strength and hybridization.

Paper VI examines pressure induced iron spin state transition in $FeCO_3$ using iron $K\beta$ x-ray emission spectroscopy. $FeCO_3$ is more compressible than iron monoxide and a magnetic transition was discovered at around 50 GPa during the experiment, compared to the transition pressure of 140 GPa in FeO. Pressure induced phase transitions in iron minerals are relevant for geophysical models of deep earth phenomena [43,112,113]. $FeCO_3$ was determined to be a prominent candidate for extending both experimental and theoretical studies of these systems especially as the iron concentration is relatively high and the mineral does not contain heavy atoms, which would result in high sample self-absorption during the x-ray scattering process. In **paper VI**, iron $K\beta$ x-ray emission was measured from $FeCO_3$ sample under high pressure conditions from ambient to 88 GPa pressure. The pressure induced evolution of the emission spectra was analyzed using the IAD approach. The paper also provides charge transfer multiplet calculations of the low and high pressure phase $K\beta$ spectra. The iron ions were confirmed to be at HS ground state at low pressures and a relatively sharp transition to a LS state was found to take place at around 50 GPa pressures. **Paper VI** provides the first evidence for a pressure induced spin state transition in $FeCO_3$.

6 Concluding Remarks

This thesis describes recent developments in x-ray Raman and x-ray emission spectroscopy with applications to MgB_2 superconductors and spin phase transitions in strongly correlated transition metal oxide systems. The experimental work required the use of a third generation synchrotron radiation source beamline equipped with a crystal spectrometer for eV energy resolution analysis of the scattered radiation. For both XRS and x-ray emission experiments one of the main advancements has been the development of these techniques to more quantitative analysis tools. One can now extract the angular symmetry components of the final state density of the empty electron states from the experimental XRS spectra. In x-ray emission spectroscopy the lineshape analysis is giving a quantitatively access to the spin magnetic moment of the emitting transition metal ion. Both of these methods have been applied and critically examined in this thesis. Upcoming experiments in both XRS and x-ray emission field will benefit from the spectrometers equipped with multiple analyzer crystals. These developments in the analysis methods and in the instrumentation will possibly enable both of these spectroscopies to become more routine analysis tools for a wider range of scientific research.

Studies of MgB_2 systems will continue to be very topical in the near future. Discerning the effects of different atomic substitutions on the electronic structure will provide challenges for the utilization of XRS in the studies of this interesting superconductor. High pressure physics using the diamond anvil cell will also certainly be a highly interesting field offering prospects for a meaningful multidisciplinary research. The usability of x-ray techniques in this field would seem to make efforts to further extend XRS technique to high pressure studies a worthwhile undertaking.

The experimental work presented in this thesis has been complemented by theoretical modeling of the x-ray spectra and the electronic structure using computational methods. The computational work has been crucial in all the presented cases to fully exploit the experimental results: to understand the origin of the different spectral features and to relate them to the electronic structure of the studied systems. Especially the cluster multiplet model was systematically applied to calculate the $K\beta$ emission line from various transition metal oxide systems. It will be interesting to see if future developments will lead to a practical first principles approach for predicting the different x-ray spectra of these strongly correlated systems.

References

[1] W. C. Röntgen, Sitzungsberichte Phys. Mediz. Gesellschaft zu Würzburg **137**, 132 (1895); English translation in Nature **53**, 274 (1896).

[2] H. G. J. Moseley, Phil. Mag. **26**, 1024 (1913).

[3] C. G. Barkla, Phil. Mag. **22**, 396 (1911); C. G. Barkla and V. Collier, Phil. Mag. **23**, 987 (1912).

[4] A. H. Compton, Phys. Rev. **21**, 207 and 483 (1923).

[5] P. Debye, Physikalische Zeitschrift **24**, 165 (1923).

[6] J. W. M. Dumond, Phys. Rev. **33**, 643 (1929).

[7] W. Stenström, Ann. Phys. (Leipzig) **57**, 347 (1918).

[8] H. Fricke, Phys. Rev. **16**, 202 (1920).

[9] W. Kossel, Z. Phys. **1**, 119 (1920).

[10] Y. Mizuno and Y. Ohmura, J. Phys. Soc. Jpn. **22**, 445 (1967).

[11] A. L. Robinson, in *X-ray data booklet*, 2nd edition, chapter 2.2 (Lawrence Berkeley National Laboratory, California, 2001).

[12] H. A. Kramers and W. Heisenberg, Z. Phys. **31**, 681 (1925).

[13] See for example W. Schülke in *Handbook on Synchrotron Radiation*, Vol. 3, edited by G. Brown and D. E. Moncton (North Holland, Amsterdam, 1991).

[14] L. Van Hove, Phys. Rev. **95**, 249 (1954).

[15] S. Manninen and K. Hämäläinen, Phys. Rev. B **45**, R3878 (1992).

[16] H. Nagasawa, S. Mourikis, and W. Schülke, J. Phys. Soc. Jpn. **66**, 3139 (1997).

[17] C. Brouder, J. Phys.:Condens. Matter **2**, 701 (1990).

[18] W. L. Mao, H.-K. Mao, P. J. Eng, T. P. Trainor, M. Newville, C.-C. Kao, D. L. Heinz, S. Shu, Y. Meng, and R. J. Hemley, Science **203**, 425 (2003).

[19] Y. Meng, H.-K. Mao, P. Eng, T. R. Trainor, M. Newville, M. Y. Hu, C.-C. Kao, J. Shu, D. Hausermann, and R. J. Hemley, Nature Materials **3**, 111 (2004).

[20] D. T. Bowron, M. H. Krisch, A. C. Barnes, J. L. Finney, A. Kaprolat, and M. Lorenzen, Phys. Rev. B **62**, R9223 (2000).

[21] J. Fink in *Unoccupied Electronic States, Fundamentals for XANES, EELS, IPS and BIS*, edited by J. C. Fuggle and J. E. Inglesfield (Springer-Verlag, Berlin, 1992).

[22] J. Stöhr, *NEXAFS spectroscopy, Springer Series in Surface Science 25* (Springer, New York, 1996).

[23] Y. Zhu, A. R. Moodenbaugh, G. Schneider, J. W. Davenport, T. Vogt, Q. Li, G. Gu, D. A. Fischer, and J. Tafto, Phys. Rev. Lett. **88**, 247002 (2002).

[24] A. P. Hitchcock, J. Electron Spec. Relat. Phenom. **112**, 9 (2000).

[25] S. Doniach, P. M. Platzman, and J. T. Yue, Phys. Rev. B **4**, 3345 (1971).

[26] M. H. Krisch, F. Sette, C. Masciovecchio, and R. Verbeni, Phys. Rev. Lett. **78**, 2843 (1997).

[27] K. Hämäläinen, S. Galambosi, J. A. Soininen, E. L. Shirley, J.-P. Rueff, and A. Shukla, Phys. Rev. B **65**, 155111 (2002).

[28] C. Sternemann, M. Volmer, J. A. Soininen, H. Nagasawa, M. Paulus, H. Enkisch, G. Schmidt, M. Tolan, and W. Schülke, Phys. Rev. B **68**, 035111 (2003).

[29] C. Sternemann, J. A. Soininen, S. Huotari, G. Vankó, M. Volmer, R. A. Secco, J. S. Tse, and M. Tolan, Phys. Rev. B **72**, 035104 (2005).

[30] J. A. Soininen, A. L. Ankudinov, and J. J. Rehr, Phys. Rev. B **72**, 045136 (2005).

[31] A. L. Ankudinov, B. Ravel, J. J. Rehr, and S. D. Conradson, Phys. Rev. B **58**, 7565 (1998).

[32] J. A. Soininen, J. J. Rehr, A. Mattila, S. Galambosi, and K. Hämäläinen, AIP Conf. Proc. **88**, 102 (2007).

[33] J. A. Bearden, Rev. Mod. Phys. **39**, 78 (1967).

[34] M. O. Krause and J. H. Oliver, J. Phys. Chem. Ref. Data **8**, 329 (1979).

[35] P. Glatzel and U. Bergmann, Coord. Chem. Rev. **249**, 65 (2005).

[36] See, for example A. Kotani, Eur. Phys. J. B **47**, 3 (2005).

[37] K. Hämäläinen, C.-C. Kao, J. B. Hastings, D. P. Siddons, L. E. Berman, V. Stojanoff, and S. P. Cramer, Phys. Rev. B **46**, 14274(R) (1992).

[38] G. Peng, X. Wang, C. R. Randall, J. A. Moore, and S. P. Cramer, Appl. Phys. Lett. **65**, 2527 (1994).

[39] S. Sugano, Y. Tanabe, and H. Kamimura, *Multiplets of Transition Metal Ions in Crystals* (Academic Press, London, 1970).

[40] H. Bethe, Ann. Physik **3**, 133 (1929).

[41] J.-P. Rueff, M. Krisch, Y. Q. Cai, A. Kaprolat, M. Hanfland, M. Lorenzen, C. Masciovecchio, R. Verbeni, and F. Sette, Phys. Rev. B **60**, 14510 (1999).

[42] J.-P. Rueff, A. Shukla, A. Kaprolat, M. Krisch, M. Lorenzen, F. Sette, and R. Verbeni, Phys. Rev. B **63**, 132409 (2001).

[43] J. Badro, J.-P. Rueff, G. Vankó, G. Monaco, G. Fiquet, and F. Guyot, Science **305**, 383 (2004).

[44] P. Glatzel and U. Bergmann, Coord. Chem. Rev. **249**, 65 (2005).

[45] G. Vankó, T. Neisius, G. Molnár, F. Renz, S. Kárpáti, A. Shukla, and F. M. F. de Groot, J. Phys. Chem. B **110**, 11647 (2006).

[46] G. Vankó and F. M. F. de Groot, Phys. Rev. B **75**, 177101 (2007).

[47] T. E. Westre, P. Kennepohl, J. G. DeWitt, B. Hedman, K. O. Hodgson, and E. I. Solomon, J. Am. Chem. Soc. **199**, 6297 (1997).

[48] G. van der Laan, B. T. Thole, G. A. Sawatzky, and M. Verdaguer, Phys. Rev. B **37**, 6587 (1988).

[49] F. M. F. de Groot, *PhD thesis* (University of Nijmegen, 1991).

[50] F. M. F. de Groot, J. Electron Spectrosc. Relat. Phenom. **67**, 529 (1994).

[51] G. Onida, L. Reining, and A. Rubio, Rev. Mod. Phys. **74**, 601 (2002).

[52] J. Kübler and V. Eyert *in Material Science and Technology, A Comprehensive treatment*, Vol 3A, edited by R. W. Kahn, P. Haasen, and E. J. Kramer (Weinheim, New York, 1991).

[53] J. J. Rehr and R. C. Albers, Rev. Mod. Phys. **72**, 621 (2000).

[54] L. Campbell, L. Hedin, J. J. Rehr, and W. Bardyszewski, Phys. Rev. B **65**, 064107 (2002).

[55] W. Kohn and L. J. Sham, Phys. Rev. A, **140**, 1133 (1965).

[56] L. Hedin and B. I. Lundqvist, J. Phys. C **4**, 2064 (1971).

[57] A. Ankudinov and J. J. Rehr, Comput. Phys. Commun. **98**, 359 (1996).

[58] L. Mattheiss, Phys. Rev. **133**, A1399 (1964).

[59] H. Sternemann, J. A. Soininen, C. Sternemann, K. Hämäläinen, and M. Tolan, Phys. Rev. B **75**, 075118 (2007).

[60] S. Galambosi, M. Knaapila, J. A. Soininen, K. Nygård, S. Huotari, F. Galbrecht, U. Scherf, A. P. Monkman, and K. Hämäläinen, Macromolecules **39**, 9261 (2006).

[61] P. W. Anderson, Phys. Rev. **115**, 2 (1959).

[62] T. Jo and A. Kotani, J. Phys. Soc. Jpn. **57**, 2288 (1988).

[63] A. Fujimori and F. Minami, Phys. Rev. B **30**, 957 (1984).

[64] O. Gunnarsson and K. Schönhammer, Phys. Rev. B **28**, 4315 (1983).

[65] G. A. Sawatzky and J. W. Allen, Phys. Rev. Lett **53**, 2339 (1984).

[66] J. Zaanen, G. A. Sawatzky, and J. W. Allen, Phys. Rev. Lett. **55**, 418 (1985).

[67] G. van der Laan, J. Zaanen, G. A. Sawatzky, R. Karnatak, and J.-M. Esteva, Phys. Rev. B **33**, 4253 (1986).

[68] A. Kotani and S. Shin, Rev. Mod. Phys. **73**, 203 (2001).

[69] F. M. F. de Groot, Chem. Rev. **101**, 1779 (2001).

[70] F. M. F. de Groot, Coord. Chem. Rev. **249**, 31 (2005).

[71] R. D. Cowan, *The theory of atomic structure and spectra* (University of California Press, Berkeley, 1981).

[72] P. Butler, *Point Group Symmetry Applications: Methods and Tables* (Plenum Press, New York, 1981).

[73] K. Okada, A. Kotani, H. Ogasawara, Y. Seino, and B. T. Thole, Phys. Rev. B **47**, 6203 (1993).

[74] M. Taguchi, T. Uozumi, and A. Kotani, J. Phys. Soc. Jpn. **66**, 247 (1997).

[75] P. Glatzel, U. Bergmann, F. M. F. de Groot, and S. P. Cramer, Phys. Rev. B **64**, 045109 (2001).

[76] S. P. Cramer, F. M. F. de Groot, Y. Ma, C. T. Chen, F. Sette, C. A. Kipke, D. M. Eichhorn, M. K. Chan, W. H. Armstrong, E. Libby, G. Christou, S. Brooker, V. Mckee, O. C. Mullins, and J. C. Fuggle, J. Am. Chem. Soc. **113**, 7937 (1991).

[77] S. Butorin, J. Electron Spectrosc. Relat. Phenom. **110**, 213 (2000).

[78] U. Bergmann, P. Glatzel, and S. P. Cramer, Microchem. J. **71**, 221 (2002).

[79] T. T. Fister, G. T. Seidler, L. Wharton, A. R. Battle, T. B. Ellis, J. O. Cross, A. T. Macrander, W. T. Elam, T. A. Tyson, and Q. Qian, Rev. Sci. Instrum. **77**, 063901 (2006).

[80] S. Huotari, private communication; S. Huotari, F. Albergamo, G. Vankó, R. Verbeni, and G. Monaco, Rev. Sci. Instrum. **77**, 053102 (2006).

[81] A. Jayaraman, Rev. Mod. Phys. **55**, 65 (1983).

[82] J. Xu, H.-K. Mao, R. J. Hemley, and E. Hines, Rev. Sci. Instrum. **75**, 1034 (2004).

[83] H.-K. Mao and P. M. Bell, Science **200**, 1145 (1978); Carnegie Institution of Washington Year Book **77**, 904 (1978).

[84] Y. K. Vohra, H. Xia, H. Luo, and A. L. Ruoff, Appl. Phys. Lett. **57**, 1007 (1990).

[85] D. J. Dunstan, Rev. Sci. Instrum. **60**, 3789 (1989).

[86] R. Miletich, D. R. Allan, and W. F. Kuhs, Rev. Mineral. Geochem. **41**, 445 (2001).

[87] R. A. Forman, G. J. Piemarini, J. D. Barnett, and S. Block, Science **176**, 284 (1972).

[88] Y. Akahama and H. Kawamura, J. Appl. Phys. **96**, 3748 (2004).

[89] J.-P. Rueff, A. Mattila, J. Badro, G. Vankó, and A. Shukla, J. Phys.: Condens. Matter **17**, S717 (2005).

[90] J. A. Xu and H.-K. Mao, Science **290**, 783 (2000).

[91] S. Deemyad, E. Sterer, C. Barthel, S. Rekhi, J. Tempere, and I. F. Silvera, Rev. Sci. Instrum. **76**, 125104 (2005).

[92] A. Dadashev, M. P. Pasternak, G. K. Rozenberg, and R. D. Taylor, Rev. Sci. Instrum. **72**, 2633 (2001).

[93] J. Nagamatsu, N. Nakagawa, T. Muranaka, Y. Zenitani, and J. Akimitsu, Nature (London) **410**, 63 (2001).

[94] J. Bardeen, L. N. Cooper, and J. R. Schrieffer, Phys. Rev. **108**, 1175 (1957).

[95] A. Y. Liu, I. I. Mazin, and J. Kortus, Phys. Rev. Lett. **87**, 087005 (2001).

[96] H. J. Choi, D. Roundy, H. Sun, M. L. Cohen, and S. G. Louie, Nature (London) **418**, 758 (2002); Phys. Rev. B **66**, 020513(R) (2002).

[97] I. I. Mazin, O. K. Andersen, O. Jepsen, O. V. Dolgov, J. Kortus, A. A. Golubov, A. B. Kuzmenko, and D. van der Marel, Phys. Rev. Lett. **89**, 107002 (2002).

[98] For a review, see special issue on MgB_2, Physica C **385**, 1 (2003).

[99] J. M. An and W. E. Pickett, Phys. Rev. Lett. **86**, 4366 (2001).

[100] T. Yildirim, O. Gulseren, J. W. Lynn, C. M.Brown, T. J. Udovic, Q. Huang, N. Rogado, K. A. Regan, M. A. Hayward, J. S. Slusky, T. He, M. K. Haas, P. Khalifah, K. Inumaru, and R. J. Cava, Phys. Rev. Lett. **87**, 037001 (2001).

[101] E. L. Shirley, Phys. Rev. Lett. **80**, 794 (1998).

[102] J. A. Soininen and E. L. Shirley, Phys. Rev. B **64**, 165112 (2001).

[103] R. S. Gonnelli, D. Daghero, G. A. Ummarino, A. Calzolari, M. Tortello, V. A. Stepanov, N. D. Zhigadlo, S. M.Kazakov, and J. Karpinski, J. Supercond. **18**, 681 (2005).

[104] R. S. Gonnelli D. Daghero, G. A. Ummarino, A. Calzolari, V. Dellarocca, V. A. Stepanov, S. M.Kazakov, J. Jun, and J. Karpinski, J. Phys. Chem. Solids, **67**, 360 (2006).

[105] J. Karpinski, N. D. Zhigadlo, G. Schuck, S. M. Kazakov, B. Batlogg, K. Rogacki, R. Puzniak, J. Jun, E. Muller, P. Wagli, R. Gonnelli, D. Daghero, G. A. Ummarino, and V. A. Stepanov, Phys. Rev. B **71**, 174506 (2005).

[106] S. M. Kazakov, R. Puzniak, K. Rogacki, A. V. Mironov, N. D. Zhigadlo, J. Jun, C. Soltmann, B. Batlogg, and J. Karpinski, Phys. Rev. B **71**, 024533 (2005).

[107] J. Kortus, O. V. Dolgov, R. K. Kremer, and A. A. Golubov, Phys. Rev. Lett. **94**, 027002 (2005).

[108] A. Carrington, J. D. Fletcher, J. R. Cooper, O. J. Taylor, L. Balicas, N. D. Zhigadlo, S. M. Kazakov, J. Karpinski, J. P. H. Charmant, and J. Kortus, Phys. Rev. B **72**, 060507(R) (2005).

[109] R. H. Potze, G. A. Sawatzky, and M. Abbate, Phys. Rev. B **51**, 11501 (1995).

[110] H. G. Drickamer, C. W. Frank, and C. P. Slichter, Proc. Natl. Acad. Sci. USA **69**, 933 (1972).

[111] A. Shukla, J.-P. Rueff, J. Badro, G. Vankó, A. Mattila, F. M. F. de Groot, and F. Sette, Phys. Rev. B **67**, 081101(R) (2003).

[112] J. Badro, G. Fiquet, F. Guyot, J.-P. Rueff, V. V. Struzhkin, G. Vankó, and G. Monaco, Science **300**, 789 (2003).

[113] J.-F Lin, V. V. Struzhkin, S. D. Jacobsen, M. Y. Hu, P. Chow, J. Kung, H. Liu, H.-K. Mao, and R. J. Hemley, Nature **436**, 377 (2005).